Impact of Hall Thruster Harness Impedance on Time-Resolved Ion Energy

IEPC-2025-068

Presented at the 39th International Electric Propulsion Conference Imperial College London • London, United Kingdom 14-19 September 2025

Austen Thomas¹ and Kristina Lemmer²
Western Michigan University, Kalamazoo, MI, 49008, USA

Abstract: The impact of HET (Hall effect thruster) harnessing inductance on discharge telemetry and plume properties was investigated by varying the harness inductance using an air core roller inductor. In this study, we evaluate a range of harness inductances using a 300-W HET while measuring time-resolved ion energy and plasma potential with a high-speed retarding potential analyzer and a high-speed dual Langmuir probe, respectively. Diagnostics were translated between two positions 0.5-m downstream of the thruster, with both positions fixed at and oriented toward the thruster centerline. This work reveals that harness inductance influences ion energy populations in HET plumes, leading to energy shifts and an increased fraction of higher-energy ions at greater harness impedances, underscoring its importance in thruster-facility electrical configuration.

Nomenclature

A = Aperture area

D = Embedding dimension

C = Total harness capacitance

E = Ion energy

e = Elementary charge f = Distribution function I_{coll} = Collector current I_c = Capacitor current I_d = Discharge current

 I_{max} = Maximum collector current I_s = Power supply current k = Nearest neighbors

L = Total harness inductance

 m_i = Ion mass N = Sample depth n_i = Ion density

R = Total harness resistance T_e = Electron temperature V_A = Anode voltage V_{bias} = Retarding potential V_p = Plasma potential V_s = Power supply voltage θ = Scattering angle

² Professor, Mechanical & Aerospace Engineering, kristina.lemmer@wmich.edu



The 39th International Electric Propulsion Conference, Imperial College London, London, United Kingdom 14-19 September 2025

¹ PhD candidate, Mechanical & Aerospace Engineering, austen.j.thomas@wmich.edu

I. Introduction

Hall effect thrusters (HETs) have long been recognized as a primary means of electric propulsion for in-space applications, with growing interest driven by the development of higher-power variants. While these thrusters operate using direct current (DC) power sources, they experience a wide range of plasma oscillations, spanning frequencies ranging from 1 kHz to tens of MHz. The dynamic behavior of HETs has prompted significant research into how various plasma oscillations impact HET performance and longevity. However, it is important to recognize that the plasma oscillations observed in HETs are not solely a function of the thruster design itself. Facility effects—such as variations in electrical configuration, background pressure, and chamber constraints—can also alter the behavior of these oscillations [1–7]. The electrical configuration encompasses how the thruster body is electrically tied, the discharge filter, and power harnessing. The discharge filter, typically comprised of passive circuit elements, is used to suppress low-frequency current oscillations between the discharge supply and the thruster. The power harness refers to the cables and electrical connectors that deliver power from the discharge supply to the thruster. Among these elements, Piñero demonstrated that variations in the power harness length affect discharge oscillations through changes in harnessing impedance [8]. This investigation concluded that inductance, in particular, contributes to an increase in both peak-to-peak amplitude and RMS discharge voltage oscillations at the anode.

The investigation conducted by Piñero was supported by a power supply model developed by Brieda *et al.*, showing agreement between both experimental and simulated results [9]. The model was used to predict the impact of cable length on HET discharge voltage oscillations, where voltage oscillations at the anode can be related to the harness electrical properties as depicted in Eq. (1).

$$V_{\rm S} - RI_{\rm S} - L\frac{dI_{\rm S}}{dt} = V_{\rm A},\tag{1}$$

where V_s is the power supply voltage, V_A is the anode voltage, R is the total harness resistance, and L is the total harness

inductance. The current supplied to the thruster is defined as $I_s = I_c + I_d$, where I_c is the capacitor current, and I_d is the discharge current. An illustration of this model is shown in Fig. 1. The current through the capacitor, with a total capacitance C, is described by $I_c = C \, dV_A/dt$. From this simple model, it is evident that the third term on the left-hand-side of Eq. (1), representing the product of the inductance and the rate of change of the supply current, can significantly influence the oscillatory nature of the discharge voltage. As the value of L increases, the magnitude of the RMS anode voltage oscillation will to increase as well.

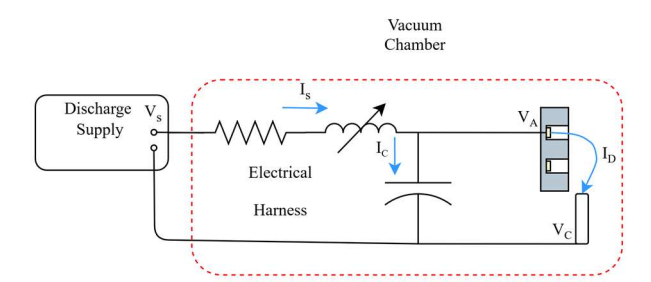


Figure 1. Electrical harness power supply model.

The harnessing configurations differ between grounded testing facilities and operation in space onboard a spacecraft bus. Understanding the influence of harness impedance on HET operation is essential, as discrepancies between ground-based and in-space harness setups may lead to unexpected thruster behavior. To fully characterize the impact of harness inductance, time-resolved measurements of thruster discharge telemetry and plume properties are required. While time-averaged measurements provide useful insight into HET performance and operation, they cannot capture the temporal dynamics critical to understanding HET operation. Hall effect thrusters exhibit a wide range of plasma oscillations, with frequencies spanning from 1 kHz to tens of MHz. In this study, we evaluate a range of harness inductances using a 300-W HET while measuring time-resolved plasma properties. This allows us to quantify the impact of harness inductance on HET plume properties.



II. Experimental Setup

A. Facility

All testing was conducted at Western Michigan University in the Aerospace Laboratory for Plasma Experiments (ALPE), utilizing the Cold Plasma Experimental Research Station (CEReS), a 1.0-m-diameter by 1.5-m-long cylindrical vacuum chamber. Pressure within the facility was monitored using two vacuum gauge controllers: an Instrutech B-RAX 3200 and a Terranova Model 934, each operating a Bayard-Alpert ion gauge. High-vacuum was achieved through the use of two cryogenic pumps, the Edwards Vacuum CTI-250F and CTI-10, obtaining a base pressure on the order of 1 x 10⁻⁷ Torr-N₂. Xenon propellant was supplied to the anode and cathode of the HET through two ALICAT mass flow controllers. To modify HET Harness inductance, an air core roller inductor was integrated in-line with the anode supply, providing four set points: 3.95 μH, 5.15 μH, 7.15 μH, and 9.15 μH.

B. Test Article

Testing was conducted using the SPT-50, a 300-W HET with a 50mm-external diameter channel, developed by the Research Institute of Applied Mechanics and Electrodynamics of Moscow Aviation Institute [10, 11]. The ALPE heaterless cathode (AHC-3.2) served as an externally mounted electron source for the SPT-50 [12]. Figure 2 shows the HET and cathode operating in CERES prior to testing. For the presented work, the SPT-50 was operated at a single condition, 240-W (200 V, 1.2 A) for the entire duration of the experiment with the thruster body electrically connected to cathode common, as shown in Fig. 1. The anode and cathode flow rates were held at 12 sccm and 2.4 sccm, respectively, resulting in an operational pressure of 9.5 x 10⁻⁵-Xe. The thruster was centrally mounted along the axis of the vacuum facility and fired downstream toward the diagnostic setup. To monitor the time-resolved telemetry of the thruster, a Viktrex VCS40 current sensor, 410 Pearson coil, and a Micsig DP10013 high-voltage differential probe were utilized, allowing data to be sampled at 50 MHz by a 16-bit digitizer.



Figure 2. SPT-50 operating in ALPE.

C. Diagnostics

The diagnostics used in this investigation, including a high-speed retarding potential analyzer (HSRPA) and a high-speed dual Langmuir probe (HDLP), were mounted on an 80/20 T-slotted frame and placed on a 2-axis motion stage system. A linear stage was used to move between two locations 0.5-m downstream of the thruster fixed at thruster centerline height, while a second rotational stage was utilized to direct the diagnostics toward the thruster centerline. The first measurement location, referred to as position #1, was offset 0.2-m radially from the centerline, and the second, position #2, was directly at the thruster centerline. Temporal measurements were conducted using the HSRPA and HDLP to obtain time-resolved ion energy distribution functions (IEDFs) and time-resolved plasma potential measurements, respectively. A transimpedance amplifier (TIA) was mounted to the back of the RPA within the vacuum chamber, allowing line capacitance to be minimized between the RPA and TIA. Each diagnostic is discussed further in the following sections.

i. High-Speed Retarding Potential Analyzer

An RPA operates by establishing a variable electric field normal to incoming ions, creating a potential barrier that filters ions with energy lower than the sourced potential. The electric field within an RPA is formed by a series of mesh grids biased to various potentials. The RPA utilized in this study features a four-grid configuration, consisting of three electrostatically biased mesh grids and a floating grid, located upstream of a current collection plate. The body, grids, retention rings, and wires are composed of 316 stainless steel. MACOR washers and a MACOR inner sleeve are used to insulate the grids from the RPA body and each other, while alumina tubing insulates the wires connected to the grids. Figure 3 shows a schematic of the RPA. Grid #1 is floating to minimize disturbance to the plasma from the biased grids and to limit space charge effects in the RPA. Grid #2 is negatively biased to repel plasma-born electrons from entering the RPA. Grid #3 is the retarding grid and is responsible for filtering ions. Grid



#4 is biased negatively to suppress electron emission from the grids and collector due to the impact of high-energy ions. The RPA utilized in this investigation possesses an energy resolution, as determined by the geometry of the RPA grids, of approximately 1.5% of the retarding grid potential [13]. Further details on the construction of the RPA can be found in Ref. [14].

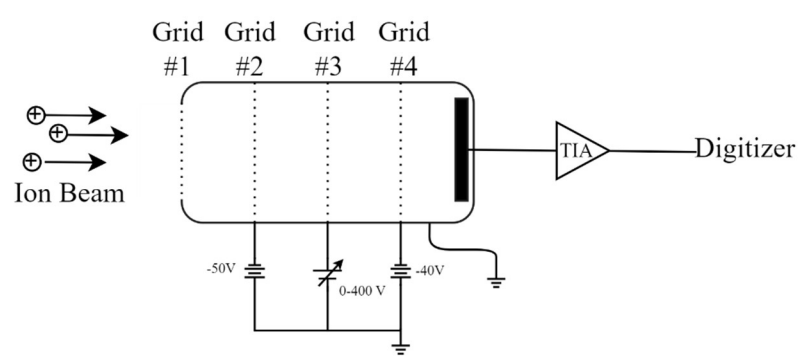


Figure 3. Retarding potential analyzer setup.

A standard RPA operates by sweeping the retarding grid over a range of positive potentials, filtering ions based on their energy per unit charge, E/q. Ions possessing energy exceeding the retarding grid potential can overcome the potential barrier and arrive at the collector, forming a measurable current. By recording the collector current as a function of the retarding potential, an I–V characteristic curve is established. The IEDF is commonly approximated solely as the negative derivative of the collector current with respect to the retarding grid bias $f(E) \approx -dI_{coll}/V_{bias}$. However, the exact formulation is given by Eq. (2),

$$-\frac{dI_{coll}}{dV_{bias}} = Aen_i \sqrt{\frac{2E}{m_i}} f(E).$$
 (2)

The measured IEDF requires correction for the local plasma potential, as the retarding grid of the RPA is ground-referenced. The true ion energy from the RPA is calculated using Eq. (3).

$$E = eV_{bias} - eV_p \tag{3}$$

Measurements in this investigation were collected at 150 discrete retarding grid potentials, with the retarding bias profile defined as $V_{bias} = [0:2:300]$ V. A Keithley 237 source measurement unit was used to sweep the potential of the retarding grid, while the repelling and suppression grids were biased with a set of batteries to a potential of -50 V and -40 V, respectively. Collector current measurements were amplified using a FEMTO DHPCA-100 commercial TIA, and recorded using a 16-bit digitizer at 50 MS/s. Time-resolved RPA measurements were performed as follows: The retarding grid potential was held constant, as current was collected and sampled at a rate greater than the dynamics being investigated. Simultaneously, a second measurement coupled to the HSRPA collector current measurement was sampled. In this investigation, the coupled measurement is the discharge current of the HET. The retarding grid potential was then increased by the appropriate voltage step size to obtain the desired IEDF resolution. This process was repeated until a complete distribution was achieved. All time-resolved IEDFs are normalized to the local maximum for each instant in time.

Time-series data reconstruction was performed using a data fusion method known as shadow manifold interpolation (SMI), a non-linear technique based on manifold reconstruction and convergent cross-mapping (CMM), developed by Takens and Sugihara, respectively [15, 16]. In this investigation, the SMI parameters were held constant for each harness inductance setpoint to maintain consistency between reconstructions. Details on SMI and its parameters can be found in Refs. [17–19]. The reconstructed waveforms were then assembled to form I-V curves at each representative point in time. Subsequently, signal noise was reduced by applying a Savitzky–Golay filter to the data after reconstruction and a smoothing spline to the reconstructed I-V curves.



ii. High-Speed Dual Langmuir Probe

Langmuir probes provide a simple method to determine plasma properties such as plasma potential, floating potential, ion number density, electron number density, and electron temperature, by analyzing an I-V curve. The I-V curve is obtained by inserting an exposed conductor into a plasma and sweeping its applied potential. A detailed description of Langmuir probe theory and its relevance to electric propulsion can be found in Ref. [20]. By sweeping the potential of the probe at high frequencies the temporal evolution of the plasma properties can be obtained. However, complications are introduced when the probe bias is swept at high frequencies. To perform high-speed Langmuir probe measurements, additional steps are required for probe design, compensation circuitry, data collection, and data analysis. The HDLP is a two-electrode probe with each electrode spaced closely together; one electrode is

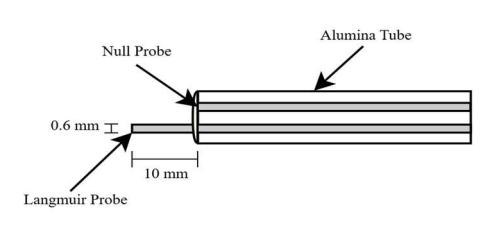




Figure 4. Diagram & constructed HDLP.

exposed to plasma, and the other, a null electrode, is insulated. In conjunction with additional circuitry, the null probe is used to compensate for capacitive distortion in the signal. Time-resolved I-V traces are obtained by sweeping both the exposed and null electrodes at a frequency such that the desired plasma dynamics can be observed and measuring the current from both the exposed electrode and null electrode. The HDLP used in this investigation, shown in Fig. 5, possesses an exposed electrode with a length of 10 mm and a diameter of 0.6 mm. The HDLP was used to estimate time-resolved plasma potential for corrections to the local plasma potential. The plasma potential is simply found by finding the maximum value of the derivative of the I-V curve measured with the HDLP. To conduct HDLP measurements, the probe was placed approximately 25 mm from the orifice of the RPA, and the potential was swept at 200 kHz while current-voltage data were sampled at 50 MS/s. In this work, the HDLP was used exclusively to obtain time-resolved plasma potential measurements, which were derived by chopping the rapidly swept current and voltage signals into discrete I-V traces and calculating the maximum derivative of each trace.

III. Results

A. Discharge Telemetry

Hall thruster discharge telemetry measurements were conducted to quantify the impact of harness inductance on discharge voltage. Discharge voltage signals are shown in Fig. 5 at each inductance setpoint. As harness inductance increased from 3.95 µH to 9.15 µH, the amplitude of the peak-to-peak discharge voltage oscillations increased by an order of magnitude, rising from 1.4 V to 15.8 V, while the mean discharge voltage remained constant at 200 V. To note, Peak-to-peak values are calculated by summing the maximum peak-to-peak value for each breathing mode period and dividing by the total number of oscillation periods. This approach was applied to all time-resolved metrics in this investigation. The primary oscillation frequency of the breathing mode varied slightly around 35 kHz, with a small downward shift of 0.3 kHz – 0.7 kHz as inductance increased. The rise in discharge voltage amplitude aligns with the relationship described in Eq. (1), agreeing with previous investigations [8, 9].

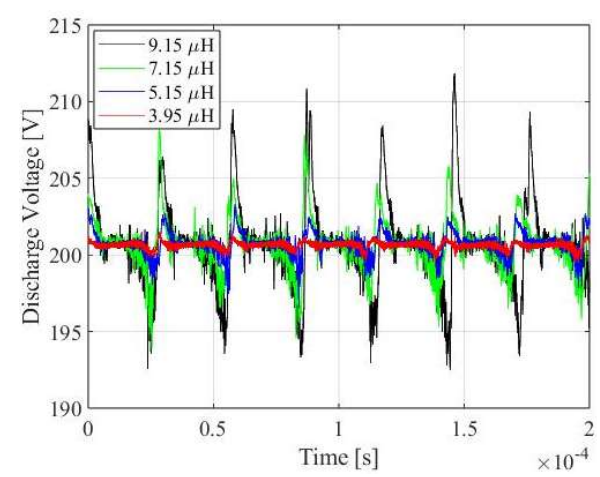


Figure 5. Hall thruster discharge voltage at various inductances.



B. Plasma Potential

High-speed plasma potential measurements were conducted using an HDLP, capturing data at each position and harness inductance setpoint. Time-averaged measurements were obtained by averaging all the highly sampled I-V traces, producing a single, averaged I-V trace for each inductance and location setpoint. By employing the methods outlined in Ref. [20], the time-averaged and time-resolved plasma potential properties are estimated and summarized in Table 1. Figure 6 depicts time-resolved plasma potential at position #2, for the 3.95 μ H and 9.15 μ H setpoints. Inspection of both time-averaged and time-resolved plasma potential measurements reveals no significant changes with increasing inductance. Indicating that plasma potential oscillations local to the RPA were unaffected by the increase in peak-to-peak discharge voltage amplitude.

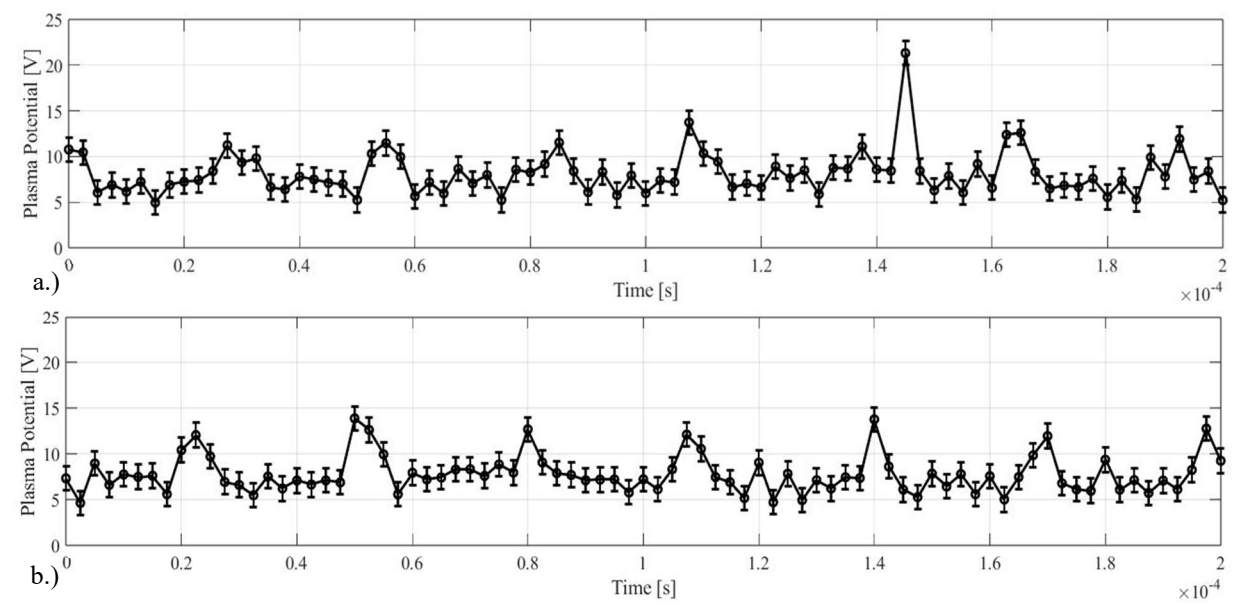


Figure 6. Plasma potential oscillations at position #2 for the a.) 3.95 μH and b.) 9.15 μH setpoints.

Table 1. Plasma potential measurements at all harness inductance setpoints.

14010	- 11 1 ms pove					
_		3.95 µH	5.15 μΗ	7.15 µH	9.15 μΗ	
Dagidian #1	V_p	8.4 V	8.6 V	8.3 V	8.1 V	
Position #1	V_{p-p2p}	5.6 V	6.0 V	5.7 V	5.5 V	
Dag:4: a.s. #2	V_p	8.2 V	8.1 V	8.0 V	7.8 V	
Position #2	V_{p-p2p}	4.6 V	4.8 V	4.7 V	4.6 V	

C. Ion Energy Distribution Function

Time-averaged ion energy measurements provide a means to assess the accuracy of time-resolved measurements and were obtained by averaging all samples collected at a single retarding bias and differentiating the averaged measured collector current with respect to the retarding bias. All IEDFs are smoothed to eliminate measurement noise. The IEDFs at each inductance condition and position are displayed in Fig. 7. Several ion energy populations exist within the HET plume, including primary beam ions, elastically scattered ions, and charge exchange (CEX) ions. The primary ion beam population is represented by a large peak near the acceleration potential, which is typically 80 – 90% of the discharge voltage; here, the discharge voltage is 200 V, resulting in an acceleration potential of around 160 eV – 180 eV [21]. Elastically scattered ions possess energy proportional to $E_b cos^2(\theta)$, where E_b is the energy of a primary beam ion and θ is the scattering angle [22]. At position #1, the RPA is 0.5-m-downstream of the HET channel exit. Under the facility operating conditions described in Section II, and assuming an ion-neutral elastic collision cross section on the order of 1 x 10⁻¹⁹ m², the mean free path for elastic collisions is estimated to be around 0.2 m – 0.9 m. This suggests that elastic collisions could plausibly account for this observed lower energy population in the range of 50 eV to 115 eV, while ions observed in the energy range on the order of 1 eV to a few 10s of eV are CEX ions.



At position #1, Fig. 7a, evidence of all three populations is visible. Primary beam ions are observed at around 178 eV, elastically scattered ions between 100 eV and 160 eV, and CEX ions below 25 eV. Examining Fig. 7b, primary beam ions show the greatest probability, with a minor contribution of CEX ions in the expected energy ranges. The time-averaged IEDFs are presented at each inductance condition, overlaid to highlight the effect on each distribution. Most notable, at position #2, was a shift in the most probable ion energy, which increased from 159 eV to 179 eV with increasing inductance. At position #1, there is a slight shift in the IEDF to higher energies of approximately 3 eV; however, this is near the measurement resolution of the RPA used in this work and, as such, may not reflect a true increase in ion energy due to harness inductance. The remaining populations apparent at position #1 do not appear to be influenced by increasing harness inductance. It is important to note, at position #1, there exists a dip at 100 eV for the 9.15 µH harness inductance case. This is the result of a mode shift to a higher discharge current condition during the HSRPA measurement period. The time-averaged IEDF features are summarized in Table 2.

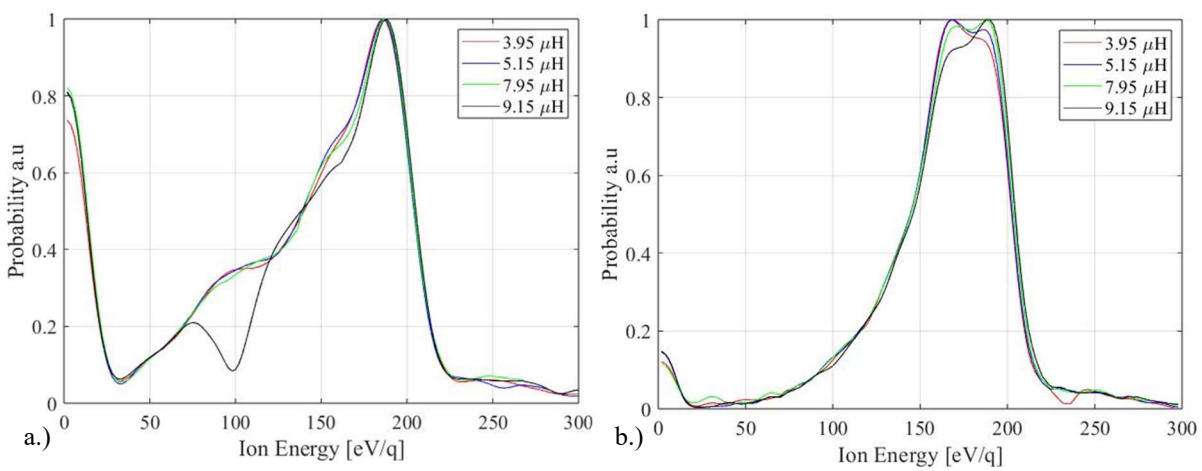


Figure 7. Time-averaged IEDFs a.) position #1 and b.) position #2 at various harness inductance setpoints.

Table 2. Time-averaged IEDF properties.

Tubic 20 Time with gen 1221 properties.							
		3.95 μΗ	5.15 μΗ	7.15 μΗ	9.15 μΗ		
	E_{i-mp}	178 eV	178 eV	180 eV	180 eV		
Position #1	E_{i-avg}	129.6 eV	128.1 eV	127.2 eV	131.0 eV		
	FWHM	64 eV	64 eV	68 eV	66 eV		
Position #2	E_{i-mp}	159 eV	159 eV	179 eV	179 eV		
	Ei-avg	153.8 eV	154.6 eV	155.0 eV	156.2 eV		
	FWHM	56 eV	56 eV	56 eV	58 eV		

Time-resolved measurements conducted in this investigation have provided insight into the influence of harness impedance on the evolving plasma dynamics within the plume of a low-power HET. Time-resolved IEDFs at each measurement location and harness inductance are displayed in Fig. 8 and Fig. 9. At position #1, the primary ion beam population oscillates at the breathing mode frequency of 35 kHz, with its energy centered around the expected acceleration potential, possessing a mean most probable ion energy of approximately ~169 eV. The average most probable energy of the primary ion beam population in all IEDFs remains constant across harness inductance values for the given energy resolution of the RPA. The magnitude of the peak-to-peak ion energy oscillations of the primary ion beam range between 44 eV and 54 eV, where peak-to-peak ion energy is defined as the range of most probable energies of the primary ion beam population. At position #1, the amplitude of the peak does not increase with harness inductance; however, the trough of the oscillation rises, resulting in a reduced peak-to-peak value. Simultaneously, a greater fraction of higher-energy ions is measured. Another interesting feature of the primary ion beam population is the shape of the most probable ion energy, becoming more square wave-like as the inductance increases. These results are discussed further in Section IV.



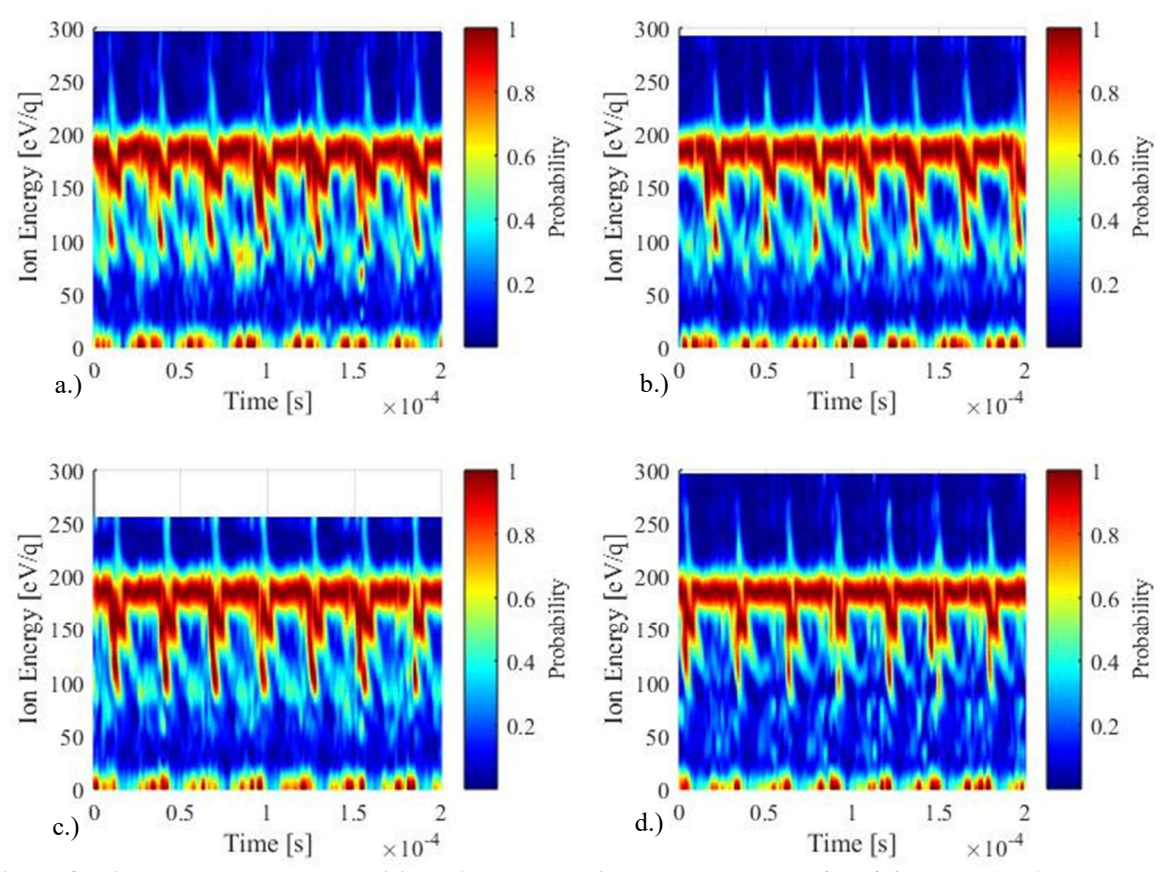


Figure 8. Time-resolved IEDFs position #1 at harness inductance values of a.) 3.95 μ H, b.) 5.15 μ H, c.) 7.15 μ H, & d.) 9.15 μ H.

In Fig. 8 the spread of energy centered around the most probable energy with a moderate probability of \sim 0.5 is akin to the full width half maximum (FWHM) of each IEDF. As the harness inductance rose from 3.95 μ H to 9.15 μ H the average FWHM value decreased by approximately 7 eV. The oscillatory nature of the discharge causes ions to cross differing potential drops around the DC acceleration potential, giving rise to this energy spread, which is only exacerbated by the increase in peak-to-peak discharge voltage amplitude as harness inductance rises. Comparing the metrics of the time-resolved IEDFs to the most probable, averaged, and FWHM of the time-averaged IEDFs reveals both similarities and key differences. The mean most probable ion energy calculated from the data reconstruction is in relatively good agreement with the time-averaged value calculated by directly averaging the HSRPA data. Minor discrepancies in average ion energy are due to data reconstruction variations. Additionally, the FHWM of both the time-averaged and time-resolved IEDFs agree well; however, the time-averaged FWHM remains constant with harness inductance, unlike the time-resolved measurement. This is possibly due to the oscillations in ion energy being averaged or smoothed out for the time-averaged analysis.

Excluding the primary ion beam population, two additional ion energy populations are observed in the time-resolved IEDFs: CEX ions in the 0–25 eV range and a second group in the 50–115 eV range. The latter is believed to result from elastic collision momentum loss but may also originate from ions formed at lower electric potentials or from CEX collisions near the end of the acceleration region. Note that the energy population in the 50 eV -115 eV range is absent at the 9.15 μ H setpoint. This is likely due to a mode shift to a lower current operating point, skewing the IEDF in this range. At the low energy spectrum of the IEDFs, 0 eV -50 eV, CEX ion populations are observed pulsating at approximately 35 kHz with both a moderate and high probability. The CEX ions were most prominent when the RPA was placed in the higher centerline angle side plume regions. This is as expected, as the literature has



shown CEX ions are more prominent near the plume edge, vacuum chamber walls, and in the background plasma behind the thruster [3, 21, 23]. With the given operating background pressure, the CEX mean free path is less than 0.2 m, smaller than the distance to the RPA, for CEX collisions to occur. While the presence of elastically scattered and CEX ions is apparent in the IEDFs, increasing harness inductance does not appear to have any significant impact on these populations.

The IEDFs at position #2, shown in Fig. 9, exhibit distinct features not present at position #1, yet they also share several characteristics similar to those observed at position #1. The IEDFs at position #2 are predominantly composed of primary beam ions, with a minor contribution from CEX ions. The average most probable energy of the primary ion beam population at position #2 is approximately 167 eV, remaining constant with increasing harness inductance, contrasting the time-averaged IEDFs. The magnitude of the ion energy oscillations of the time-resolved IEDFs increases by 4 eV - 5 eV from the lowest inductance set point with increasing inductance. However, the amplitude does not increase proportionately to the rise in discharge voltage oscillation magnitude; this discrepancy is discussed further in Section IV. The increase in ion energy oscillation amplitude is a result of ions experiencing greater instantaneous potential caused by the increased size of the discharge voltage oscillations. Measuring the effect of harness inductance on the FWHM at position #2, we can see that as inductance increases, so does the average value. Just as was discussed for position #1, this energy spread is likely the result of ions being accelerated over varying discharge potentials. The average FWHM increased by approximately 6 eV, aligning with the increase in the magnitude of the oscillations in the most probable ion energy. As for the CEX ion population, there appears to be no major impact on either its energy or temporal characteristics as a function of harness inductance. As was observed at position #1, these populations too have the temporal characteristics of the HET discharge, oscillating at the breathing mode frequency of 35 kHz.

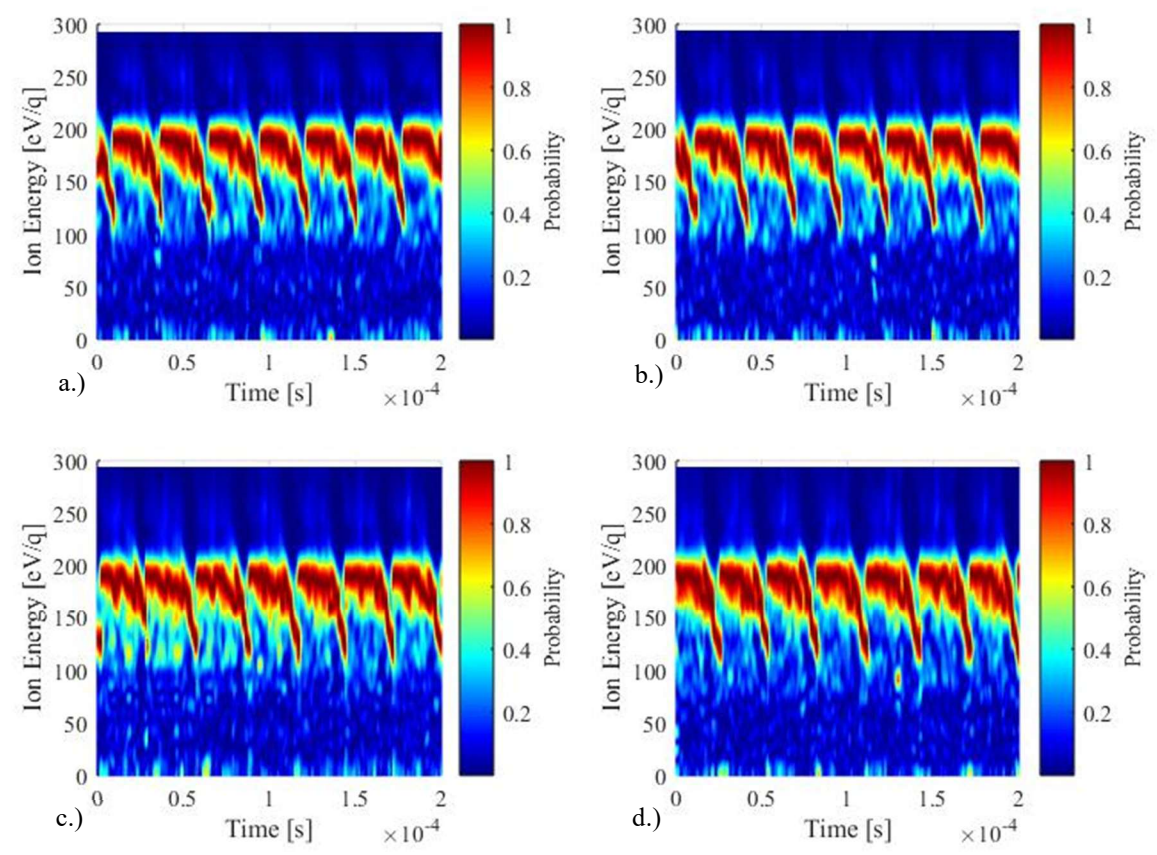


Figure 9. Time-resolved IEDFs position #2 at harness inductance values of a.) 3.95 μ H, b.) 5.15 μ H, c.) 7.15 μ H, & d.) 9.15 μ H.



Across both positions, as the harness inductance increased, the ion energy was impacted. Figure 10 and Table 3 summarize how the most probable ion energy population of each time-resolved IEDF was affected by increasing harness inductance. At position #1, the mean most probable ion energy remains constant, while the size of the oscillations in the ion energy and the average FWHM of the ion energy both decrease with increasing harness inductance. At position #2, the mean most probable ion energy remains constant, but the size of the ion energy oscillations and the average FWHM of the ion energy both increase. The most significant outcome is that an increased fraction of both higher and lower energy ions was measured as harness inductance increased.

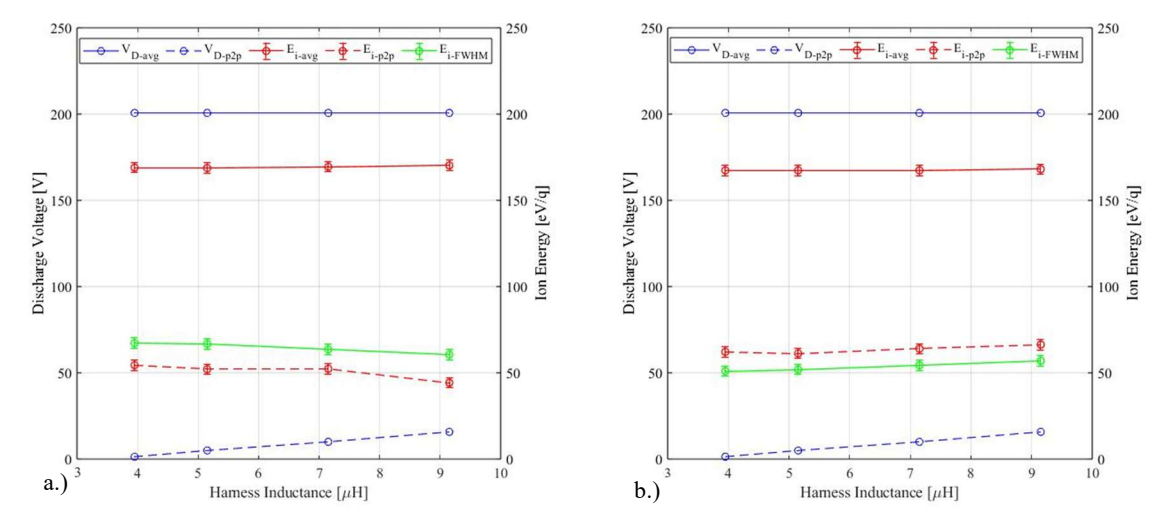


Figure 10. Impact of harness inductance on ion energy summary a.) position #1 and b.) position #2.

Table 3. Time-resolved IEDF most probable energy metrics at positions #1 and #2.

		P- 0.0000		*** P ****** ** **	
		3.95 μΗ	5.15 μΗ	7.15 µH	9.15 μΗ
Position #1	\overline{E}_{i-mp}	169.0 eV	168.7 eV	169.5 eV	170.3 eV
	E_{i-p2p}	54.5 eV	52.1 eV	52.4 eV	44.3 eV
	FWHM	67.3 eV	66.8 eV	63.6 eV	60.6 eV
	f	34.8 kHz	34.2 kHz	34.2 kHz	34.1 kHz
Position #2	\overline{E}_{i-mp}	167.4 eV	167.4 eV	167.4 eV	168.1 eV
	E_{i-p2p}	62.2 eV	61.3 eV	64.0 eV	66.4 eV
	FWHM	51.0 eV	52.0 eV	54.4 eV	57.0 eV
	f	35.2 kHz	35.2 kHz	34.8 kHz	34.8 kHz

Figure 11 compares the fraction of the most probable energy ions at the lowest and highest harness inductance setpoints, separated into four energy populations: CEX, low-energy, intermediate energy, and high-energy ions. From this figure, we can visualize which ion energy ranges are most affected by the changing harness inductance. The highlighted regions in green encompass a broad range of higher energies; however, the most pronounced changes are observed near 190 eV, where at the 9.15 μ H harness inductance setpoint, higher energy ions are more prominent. This is true for both positions. However, notable differences exist between positions and inductance setpoints. At position #1, for the 3.95 μ H setpoint, we see two energy ranges, 110 eV \pm 5 eV, highlighted in blue, and 170 eV \pm 15 eV, highlighted in yellow, where at a lower inductance setpoint, these energetic ions are more prominent. As the inductance increases, shifts toward higher energies are observed in several ranges, including a rise in the fraction of both the lowest-energy ions (CEX ions) and the highest-energy ions. At position #2, two notable outcomes in the most probable energy are observed between the lowest and highest inductance setpoints. In the lower energy range, 115 eV



- 150 eV, the most probable energies at both inductance setpoints show comparative behavior with a small increase in the probability of the lower energy tail for the 9.15 μ H set point. In the intermediate and high-energy ranges, 160 eV to 196 eV, as inductance was increased, the probability of seeing higher energy ions increased, this can be seen from the shift toward higher energies in the histogram, specifically in the 190 eV - 196 eV range. All of these results are discussed further in Section IV.

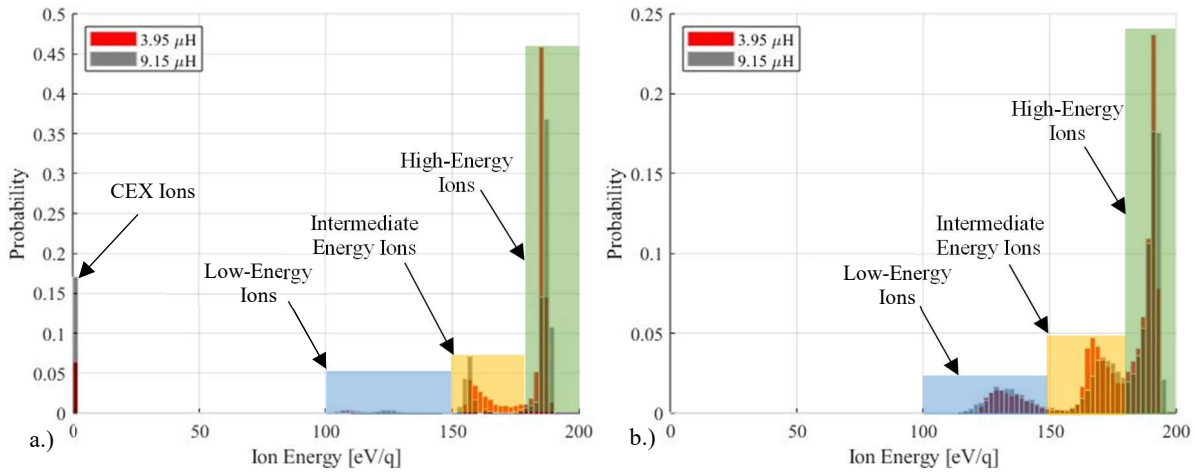


Figure 11. Most probable ion energy histogram comparison at a.) position #1 and b.) position #2.

IV. Discussion

The preceding section presented spatial measurements of time-averaged and time-resolved ion energy per charge and plasma potential within the plume of an SPT-50 HET operating on xenon at 240-W for four harness inductance setpoints: $3.95~\mu H,\, 5.15~\mu H,\, 7.15~\mu H,\, and\, 9.15~\mu H.$ As the harness inductance was changed, the different populations of ion energy varied in both time and space. Throughout each testing setpoint, plasma potential measurements were made to correct the measured ion energy for the RPA retarding grid being ground referenced. All measurements showed that the plasma potential was unaffected by changes in harness inductance.

Examining the time-averaged IEDFs, all metrics, including the most probable ion energy, average ion energy, and FWHM of the ion energy remained constant at position #1 (off-center) for any variation in harness inductance. The most probable energy at position #2 (axially aligned) showed a significant change with the harness inductance increasing by 20 eV from 3.95 μ H to 9.15 μ H. An increase in the time-averaged most probable ion energy is anticipated with the rise in ion energy amplitude. However, the observed 20 eV increase is unexpectedly large and warrants further investigation to verify its validity. While this shift in most probable ion energy is large, all IEDFs possess the same energy populations, the first at approximately 168 eV and the second at 188 eV. The increased probability of the greater energy population at the higher inductance setpoints is likely the result of a portion of ions experiencing a greater acceleration potential. If we compare the time-averaged most probable ion energy to the mean of the time-resolved most probable energy, we may expect these to agree at first; however, there is a significant difference in the values at 3.95 μ H and 5.15 μ H setpoints.

While the time-averaged and time-resolved measurements exhibit similar features, the time-resolved IEDFs provide insight into ion energy dynamics and the possible origins of thruster instabilities. Such information is important when choosing an optimum operating condition of an HET in terms of thruster performance and lifetime. Harnessing inductance has been shown to impact the temporal characteristics of the various ion energy populations measured in the time-resolved IEDFs. In the primary ion beam population, we saw increasing harness inductance resulted in an increased fraction of higher energy ions and changes in the spread of energy in terms of the magnitude



of the oscillations and the FWHM. However, these values do not increase in proportion to the rise in magnitude of the discharge voltage oscillations. Therefore, the ions within the acceleration zone must not be experiencing the full or peak acceleration potential. One possible mechanism responsible for this disproportionate rise in energy is that the peak ionization rate is not in phase with the maximum discharge voltage, resulting in fewer ions being accelerated through the highest potential drop. Work conducted by Simmonds et al. conducted a study with a modulated cylindrical hall thruster anode, through which the discharge phase could be controlled [24]. By modulating the anode voltage to resonate with the discharge current's breathing mode oscillations, Simmonds et al. altered thruster performance and shifted the phase relationship between discharge voltage, discharge current, and ion current. These phase changes increased the fraction of higher-energy ions within the plume. Additionally, they showed that when the discharge current and discharge voltage were in phase, the amplitude of the oscillations in the ion energy decreased. This modulated anode study may also explain why we did not observe a proportional rise in ion energy with discharge voltage. Whereas the modulated anode study intentionally adjusted discharge voltage to influence phase, our work examined the effects of harness inductance which likely impacted the phase of the HET discharge, altering the acceleration potential experienced by ions within the channel.

Interesting features are observed at each operating position with similarities and differences in the most probable ion energy population. At position #1, the amplitude of the ion energy oscillations decreases with increasing inductance, contrasting what was observed at position #2. However, an increased fraction of higher-energy ions was still measured at position #1, as shown in Fig. 11a. The smaller amplitude of the peak-to-peak energy is due to a shift in the energy of the most probable ion energy population in the 105 eV - 120 eV range at the $3.95 \mu\text{H}$ setpoint to the 120 eV - 130 eV range at the $9.15 \mu\text{H}$ setpoint. This mid-energy population at position #1 can also be observed in Fig. 8 as a moderate-probability feature pulsing at the breathing mode frequency in the respective energy ranges of

each inductance setpoint. Additionally, with the increased fraction of high-energy ions at the 9.15 µH setpoint, the IEDF displays a more square wave-like structure. At position #2, we saw measurable changes in the amplitude of the ion energy oscillations, the FWHM, and the oscillation frequency. These changes appear to be a direct result of increasing the harness inductance and therefore increasing the amplitude of the discharge voltage oscillations. While it may be difficult to see these changes in Fig. 9, Fig. 11b clearly shows a shift in the most probable ion energy toward higher values. Comparing the 3.95 µH to 9.15 µH setpoints, the peak in the ion energy is observed near 200 eV, oscillating with the breathing mode, as shown in Fig. 12. This feature appears to grow with increasing harness inductance and shares similar characteristics to the discharge voltage trace in Fig. 5.

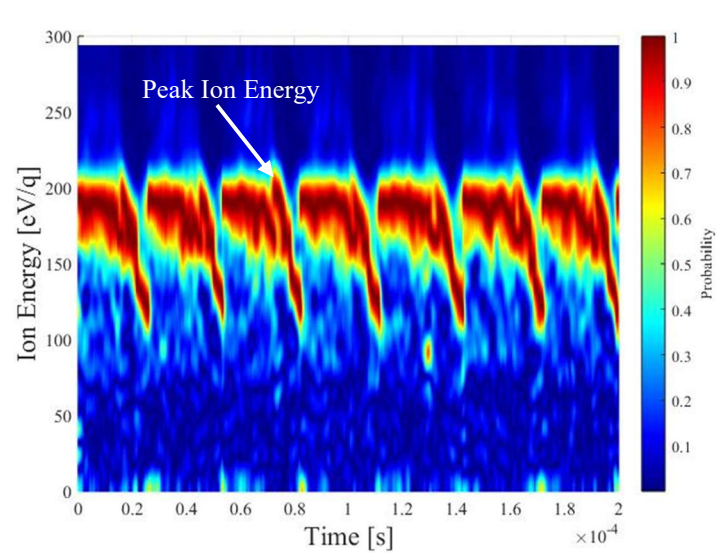


Figure 12. Time-resolved IEDF at position #2 9.15 μ H.

The remaining ion energy populations, the elastically scattered and CEX ion populations that are primarily observed only at position #1, are not significantly affected by changes in the harness inductance. However, the elastically scattered ions appear to decrease in probability while the lower energy bound increases slightly, possibly resulting from an increase in deposited AC energy into this population at greater harness inductances. While the CEX ion populations show no significant changes in energy, a greater fraction of CEX ions was measured at the higher inductance setpoint, as indicated by Fig. 11. While both the elastically scattered and CEX ions are coupled to the discharge and exhibit similar dynamics, the influence of higher energy ions on these lower energy populations is not apparent and may not be effectively transferred through collisional processes. With increasing harness inductance,



more AC power is deposited into the plasma due as indicated by the higher magnitude of the discharge voltage oscillations. These oscillations cause the primary beam ions to gain energy; however, the influence on the lower energy ions is minimal.

The results observed in this investigation highlight how the electrical configuration of a vacuum facility can influence HET operation. Each testing facility possesses a unique configuration, including differences in harnessing electrical properties such as inductance. As demonstrated in this investigation, harnessing inductance can impact both discharge telemetry and temporal plume properties. These effects are critical to consider when designing and managing the HET electrical harness, as neglecting these considerations can lead to undesirable effects on thruster performance and lifetime. Temporal measurements are essential to fully characterize the impact of harness inductance on thruster operation, as time-averaged measurements alone indicate minimal effect. The findings of this work show that greater harness inductance influences ion energy oscillations and increases the fraction of higher energy ions, which can influence thruster operation and lifetime. Recommendations for electrical harnessing have been proposed in previous studies to mitigate or prevent the effects of increased harness inductance. These recommendations include minimizing harness length, utilizing a low inductance harness alternative, such as paralleled twisted pair cable, and reducing the distance between the discharge filter capacitor and the thruster [8]. Other methods have been proposed to actively control discharge current oscillations through the implementation of proportional-integral derivative (PID) closed-loop controllers and RLC networks, effectively reducing high-amplitude discharge voltage oscillations at the anode [25–29]. Both passive and active control strategies can be implemented, either independently or in combination, to reduce discharge voltage oscillations.

V. Conclusion

Temporal measurements of HET discharge telemetry and plume properties were conducted to evaluate the impact of HET electrical harness properties on thruster operation. Time-resolved ion energy and plasma potential were measured using an HSRPA and HDLP, respectively, at two positions, 0.5-m-downstream from a 300-W HET to study ion energy populations. The results demonstrate that increasing harness inductance impacts different ion energy populations within the plume of an HET by either shifting their energy or increasing the fraction of higher energy ions present within the plume. No measurable effect was observed on the measured time-resolved plasma potential. These findings emphasize the importance of considering harness inductance during thruster qualification, as it can influence both thruster performance and lifetime. Several recommendations have been proposed to manage and reduce discharge voltage oscillations, preventing any unwanted effects due to HET electrical harnessing.

Acknowledgments

This work was partially supported by NASA through the Joint Advanced Propulsion Institute, a NASA Space Technology Research Institute, grant number 80NSSC21K1118

References

¹Jovel, D., Cabrera, J., & Walker, M. "Current Pathways Model for Hall Thruster Plumes in Ground-Based Vacuum Test Facilities: Measurements and Observations." *Journal of Electric Propulsion*, vol. 3, no. 1, 2024, p. 35, https://doi.org/10.1007/s44205-024-00097-8.

²Byrne, M., Roberts, P., & Jorns, B. "Coupling of Electrical and Pressure Facility Effects in Hall Effect Thruster Testing". Presented at the 37th International Electric Propulsion Conference. Massachusetts Institute of Technology, Cambridge, MA USA. 2022.

³Walker, J., Frieman, J., Walker, M., Khayms, V., King, D., & Peterson, P. "Electrical facility effects on hall-effect-thruster cathode coupling: Discharge oscillations and facility coupling". *J Propuls Power*, vol. 32, no. 4, pp. 844–855, 2016, doi: 10.2514/1.B35835.

⁴Frieman, J., Walker, J., Walker, M., Khayms, V., & King, D. "Electrical Facility Effects on Hall Thruster Cathode Coupling: Performance and Plume Properties". *Journal of Propulsion and Power*, vol. 32, no. 1, 2016, pp. 251–64, https://doi.org/10.2514/1.B35683.



- ⁵Peterson, P., Kamhawi, H., Huang, W., Yim, J., Herman, D., Williams, G., Gilland, J., & Hofer, R. "HERMeS Hall Thruster Electrical Configuration Characterization". *52nd AIAA/SAE/ASEE Joint Propulsion Conference, Salt Lake City, UT, July 25-27, 2016*, American Institute of Aeronautics and Astronautics (AIAA), 2016, pp. 1–1.
- ⁶Hofer, R., Peterson, P., & Gallimore, A. "Characterizing Vacuum Facility Backpressure Effects on the Performance of a Hall Thruster". Presented as Paper IEPC-01-045 at the 27th International Electric Propulsion Conference, Pasadena, CA, 15-19 October 2001.
- ⁷Macdonald, S. "Electric Propulsion Test & Evaluation Methodologies for Plasma in the Environments of Space and Testing (EP TEMPEST)." In-Space Propulsion Branch (RQRS) Aerospace Systems Directorate Edwards AFB, CA. 2016.
- ⁸Pinero, L. "The Impact of Harness Impedance on Hall Thruster Discharge Oscillations". Presented at the 35th International Electric Propulsion Conference. Georgia Institute of Technology Atlanta, GA USA. 2017
- ⁹Brieda, L., Koo, J., and Scharfe, M. "Influence of a power supply model on simulated Hall thruster discharge voltage oscillations". *AIP Adv*, vol. 9, no. 2, Feb. 2019, doi: 10.1063/1.5063440.
- ¹⁰Manzella, D., Oleson, S., Sankovic, J., Hagg, T., Semenkin, A., & Kim, V. "Evaluation of Low Power Hall Thruster Propulsion". Presented at the 32nd Joint Propulsion Conference, 1996.
- ¹¹Clauss, C., Tilley, D., & Barnhart, D. "Benefits of Low-Power Stationary Plasma Thruster Propulsion for Small Satellites". 1995.
- ¹²Mooney. M., Baird. M., & Lemmer. K. "Featherweight Heaterless Hollow Cathode Characterization". Presented at the 36th International Electric Propulsion Conference. Vienna, Austria. 2019.
- ¹³Enloe, C. "High-resolution retarding potential analyzer, Review of Scientific Instruments". vol. 65, no. 2, pp. 507–508, 1994, doi: 10.1063/1.1145167.
- ¹⁴Baird, M., Kerber, T., Lemmer, K., Huang W. "Hall Thruster Plume Measurements of Time Resolved Ion Energy". Presented at the 36th International Electric Propulsion Conference, 2019.
 - ¹⁵Takens, F. "Detecting strange attractors in turbulence". 1981, pp. 366–381. doi: 10.1007/bfb0091924.
- ¹⁶Sugihara, G., May, R., Ye, H., Hsieh, C., Deyle, E., Fogarty, M., & Munch, S." Detecting Causality in Complex Ecosystems". *Science (American Association for the Advancement of Science)*, 338(6106), 496–500. 2012. https://doi.org/10.1126/science.1227079
- ¹⁷Baird, M., McGee-Sinclair, R., Lemmer, K., & Huang, W. "Time-resolved ion energy measurements using a retarding potential analyzer". *Review of Scientific Instruments*, vol. 92, no. 7, Jul. 2021, doi: 10.1063/5.0039621.
- ¹⁸Thomas, A. & Lemmer, K. "Time-resolved Ion Energy Measurements Using a Retarding Potential Analyzer for Electric Propulsion Applications". *Rev. Sci. Inst.*, 1 February 2024; 95 (2): 023505. https://doi.org/10.1063/5.0176167
- ¹⁹Eckhardt, D., Koo, J., Martin, R., Holmes, M., & Hara, K. "Spatiotemporal data fusion and manifold reconstruction in Hall thrusters". *Plasma Sources Sci Technol*, vol. 28, no. 4, Apr. 2019, doi: 10.1088/1361-6595/ab0b1f.
- ²⁰Lobbia, R. & Beal B. "Recommended practice for use of Langmuir probes in electric propulsion testing". *Journal of Propulsion and Power, vol. 33, no. 3, 2017, pp. 566–81*, https://doi.org/10.2514/1.B35531.
- ²¹Goebel, D., Katz, I., & Mikellides, I. Fundamentals of Electric Propulsion: Ion and Hall Thrusters. 2nd ed., Wiley, 2023.
- ²²Mikellides, I., Katz, I., Kuharski, R., & Mandell, M. "Elastic Scattering of Ions in Electrostatic Thruster Plumes". *Journal of Propulsion and Power*, vol. 21, no. 1, 2005, pp. 111–118. DOI: 10.2514/1.5046.
- ²³Zhang, Z., Zhang, Z., Tang, H., Liang Ling, W., Chen, Z., Ren, J., & Cao, J. "Measurement of the distribution of charge exchange ions in a Hall-effect thruster plume". *Plasma Sources Sci Technol*, vol. 29, no. 8, Aug. 2020, doi: 10.1088/1361-6595/aba12c.
- ²⁴Simmonds, J., Raitses, Y., Smolyakov, A., & Chapurin, O. "Studies of a Modulated Hall Thruster". *Plasma Sources Science and Technology*, vol. 30, no. 6, 2021, Article 065–597, DOI: 10.1088/1361-6595/abf597
- ²⁵Barral, S., and J. Miedzik. "Numerical Investigation of Closed-Loop Control for Hall Accelerators". *Journal of Applied Physics*, vol. 109, no. 1, 2011, pp. 013302-013302-10, https://doi.org/10.1063/1.3514151.
- ²⁶Wei, L., Han, L., Ding, Y., Yu, D., & Zhang, C. "Stabilizing Low-Frequency Oscillation with Two-Stage Filter in Hall Thrusters." *Review of Scientific Instruments*, vol. 88, no. 7, 2017, p. 073502, https://doi.org/10.1063/1.4990045
- ²⁷Krishnan, A., Lev, D., Saeedifard, M., Graber, L., & Walker, M. "Impedance Analysis of the Hall Thruster Discharge Circuit and Plasma Load to Address Harness Facility Effects." *Presented at the 38th International Electric Propulsion Conference (IEPC-2024-619)*, 23–28 June 2024, Toulouse, France.



²⁸Barral, S., Miedzik, J., & Ahedo. E. "A Model for the Active Control of Low Frequency Oscillations in Hall Thrusters." *Joint Propulsion Conferences*, 15 June 2008, AIAA Paper 2008-4632.

²⁹Yu, D., Wang, C., Wei, L., Gao, C., & Yu, G. "Stabilizing of Low Frequency Oscillation in Hall

Thrusters." *Physics of Plasmas*, vol. 15, no. 11, 2008, pp. 113503-113503-07, https://doi.org/10.1063/1.3023150.

